MRS Communications

https://doi.org/10.1557/s43579-025-00719-8

MRS Communications

Methods Letter

Method for extraction of microcrystals based on focused electron/ion beam processing and their magnetotransport characterization

Amaia Sáenz-Hernández, Instituto de Nanociencia y Materiales de Aragón (INMA), CSIC-Universidad de Zaragoza, Mariano Esquillor S/N, 50018 Saragossa, Spain
Soraya Sangiao, Instituto de Nanociencia y Materiales de Aragón (INMA), CSIC-Universidad de Zaragoza, Mariano Esquillor S/N, 50018 Saragossa, Spain; Laboratorio de Microscopías Avanzadas (LMA), Universidad de Zaragoza, Mariano Esquillor S/N, 50018 Saragossa, Spain
Geetha Balakrishnan, Department of Physics, University of Warwick, Coventry CV4 7AL, UK
José María De Teresa, Instituto de Nanociencia y Materiales de Aragón (INMA), CSIC-Universidad de Zaragoza, Mariano Esquillor S/N, 50018 Saragossa, Spain

Address all correspondence to José María Teresa at **deteresa@unizar.es**

(Received 26 February 2025; accepted 15 April 2025)

Abstract

We propose a new in situ microfabrication method using focused electron/ion beam processing to study the influence of crystal orientation on magnetotransport properties. Previous studies obtained microcrystals extracted from bulk single crystals with the out-of-plane crystallographic axis $\vec{c}$ perpendicular to the applied magnetic field $\vec{B}$ and parallel to the current flow. The new method orients $\vec{c}$ parallel to $\vec{B}$ and perpendicular to the current. Magnetotransport measurements at 2 K on Bi_2Se_3 samples fabricated using both methods reveal differences in zero-field resistivity and charge carrier mobility, demonstrating the impact of the crystal orientation in which the microcrystal is extracted on the electrical transport properties.

Introduction

Generally speaking, the intrinsic properties of quantum materials are nicely observed in single crystals, but some properties such as the dependence of electrical transport properties on crystal orientation cannot be easily disentangled from studies in bulk crystals, given the large spatial distribution of the applied current. However, it is well known that due to the anisotropic crystal structure and density of states of a bulk crystal, the intrinsic electrical magnetotransport is strongly dependent on the relative orientations of the crystallographic axes, the applied current and the applied magnetic field.[1,2]

The application of focused ion beam (FIB) techniques to explore the transport properties of quantum materials is a relevant topic of research.[3] FIB is a direct-write nanolithography technique that does not require the use of chemical resists and allows precise nanofabrication, with nanometric resolution, in samples with an arbitrary surface topography. A FIB equipment accelerates and focuses an ion beam over the sample, located in a vacuum chamber, to obtain different effects. There are many sources in FIB,[4] finding Ga^+, He^+, Xe^+ and Ne^+ among the most used ones. The ion choice depends on the experiment requirements, such as resolution, sample damage, fabrication time and availability.

When ions hit the surface, they interact with atoms present in the sample causing the emission of electrons, called secondary electrons, which are collected by detectors placed inside the fabrication chamber. By counting the detected secondary electrons in each spot, a contrast image can be formed, making FIB a microscopy technique in the nanoscale. Additionally, ions transfer momentum to the surface atoms, that are sputtered away if the transferred momentum exceeds their binding energy, provoking material milling. These ions can be backscattered on the surface or implanted in it, altering the material's chemical composition and crystalline structure, causing amorphization. This is a harmful side effect in most cases but can be useful in some applications involving intentional defect creation or resists sensitive to ion irradiation.[5,6]

Material deposition is also possible when combining the ion beam with a precursor material, commonly in gas form, in a technique called Focused Ion Beam Induced Deposition (FIBID).[7] The precursor gas is formed by a non-volatile component of the material desired for deposition and a volatile part. When secondary electrons dissociate gas molecules, the volatile component is eliminated by the vacuum system and the non-volatile part remains adsorbed to the surface in the region where the beam has struck the sample. With a similar working principle, deposition is also possible when employing a Focused Electron Beam, such as that present in a Scanning Electron Microscope (SEM), in a technique called Focused Electron Beam Deposition (FEBID). The beam is controlled by the user in real time and sweeps the sample following predesigned patterns with resolution down to a few nanometers. For work requiring high-precision fabrication, equipment combining both SEM and FIB enable fabrication using the FIB while monitoring the process simultaneously with the SEM, a less harmful microscopy technique.[8]

First, we discuss the state of the art. In the past, the capability of FIB to extract lamellae from crystals has been extensively used to investigate their structural and compositional properties by means of transmission electron microscopy (TEM) experiments.[9] The methods developed include the preparation of lamellae for TEM inspections either with the ion beam parallel to the crystal slab surface (the most common method, called method 1 hereafter) or perpendicular to the slab surface (called method 2 hereafter). Method 2 is generally known as lamella for plane-view specimen view, and its preparation is more challenging than the standard one. Moll *et al*. reported a procedure to extract a small microcrystal with method 1, place it (making use of an ex situ procedure) to a prepatterned substrate with electrical contacts, and return the device to the FIB equipment for growing the electrical connections between the microcrystal and the contact pads.[10] Further FIB milling in the microcrystal allowed the authors to investigate its electrical behavior with an applied current in various crystal directions. The same group has recently shown how relevant the specific direction of the microcrystal in which the current is applied is to reveal subtle physical phenomena.[11] Other research studies have also used the advantages of FIB technology to study electrical transport properties of crystals in combination with other nanofabrication techniques. An example is the work by Mikheev *et al*. where they combined e-beam evaporation, FIB and Electron Beam Lithography (EBL) to fabricate superconducting devices.[12]

Our group has been working on further developing method 1 and method 2 and recently published a new variation of method 1 that proposes an in situ fabrication process using FIB. This publication showed that it is possible to extract a small microcrystal with method 1, transport it in situ by means of a nanomanipulator to a prepatterned substrate with electrical contacts and grow the corresponding electrical connections to investigate the magnetotransport properties of the microcrystal with the applied electrical current parallel to the out-of-plane axis of the crystal.[13] In the current article, we report our efforts developing method 2, where we extract a small microcrystal, transport it to a prepatterned substrate with electrical contacts, and perform the corresponding electrical connections to investigate the magnetotransport properties of the microcrystal with the applied electrical current being perpendicular to the out-of-plane axis of the crystal $\vec{c}$. Interestingly, if the main crystallographic axes in the surface plane are known, the method even allows for the selection of the in-plane direction along which the electrical current will be applied in the microcrystal. This new procedure complements the previous existing ones and gives access to the investigation of the magnetotransport properties with the electrical current applied parallel to the surface plane of the original bulk crystal. Additionally, in contrast with the methods reported previously, it allows us to complete the devices in situ and avoiding the use of chemical resists.

In particular, in this work, these methods have been applied to a Bi_2Se_3 single crystal as a proof-of-concept. This compound is a well-known topological insulator, an insulating material with topologically protected metallic states on its surface.[14] It has been widely studied for its potential application in quantum technologies due to its relatively long phase-coherence length l_Φ and large bandgap of $\sim$ 0.3eV.[15] This crystal has a rhombohedral structure, with atoms organized in layers inside the unit cell called the Quintuple Layer (QL), as the atoms are arranged in five different layers.[16] The atoms inside the unit cell are covalently bonded, whereas the unit cells are bonded *via* Van der Waals interactions.

Materials and methods

Materials and equipment

The Bi_2Se_3 single crystal used in this work was synthesized in the University of Warwick (UK) by the modified Bridgman method.[13]

Samples are fabricated using a Dual Beam Helios Nanolab 650 System from Thermo Fisher Scientific (Hillsboro, Oregon, USA), property of the Laboratory of Advanced Microscopies (LMA) in Zaragoza, Spain. This system features a vertically focused electron beam column, generated by a field emission gun, for Scanning Electron Microscopy (SEM)). Positioned at an angle of 52º relative to the electron column there is a Ga^+ Focused Ion Beam (FIB) column, that accelerates ions extracted from a Liquid Metal Ion Source (LMIS). Both beams, that have a maximum acceleration voltage of 30 kV, converge within a high-vacuum sample preparation chamber. The chamber is equipped with a sample holder that can rotate 180º around its vertical axis and tilt up to 57º, enabling precise orientation of the sample to interact with either beam.

Integrated within the chamber are various Gas Injection Systems (GIS) for FIBID and FEBID. Among them, the most relevant to the current work are the Pt precursor GIS ($(CH_3)_3(CpCH_3)$ Pt) and the $W(CO)_6$ one which allows W–C deposition. Another relevant accessory for this topic is the nanomanipulator, from the brand Omniprobe, which is employed for precise material transportation.

The final device will be placed on a chip made from silicon, with a 300 nm thermally grown silicon dioxide layer with prepatterned gold leads for subsequent electrical characterization. Magnetotransport measurements are performed to characterize electronic properties of the fabricated samples using a Physical Properties Measurement System (PPMS) from Quantum Design. It is a commercial system belonging to the University of Zaragoza consisting of a cryostat with a superconducting magnet coil, capable of generating magnetic fields up to 14 T where DC and AC resistivity measurements can be performed. The system can measure at a minimum temperature of 2 K with a supply of He-4 and down to 0.35 K with a He-3 insert. Samples are glued in a special puck designed for this system, using G varnish (GE/ IMI 7031 Varnish from CMRdirect), and bonded to the puck's gold pads using a micro bonding equipment through aluminum wires.

Sample preparation

The chip and crystal are positioned on the sample holder and securely fixed using a combination of copper and carbon tape. This setup prevents movement during fabrication while ensuring proper grounding to reduce charge accumulation effects during fabrication.

Both elements are introduced in the sample chamber together with a TEM lamella grid holder, where we have previously placed the grid. The grid holder is positioned horizontally on the sample holder, tilted 90º from its usual vertical orientation. Finally, the chamber is sealed, and the system is evacuated until the vacuum level reaches approximately $2 \cdot 10^{-6}$ mbar.

Extraction of the crystal slab

The extraction technique detailed in this section is based on the standard TEM lamella fabrication procedure. For the whole process, the acceleration voltage of the electron and ion beams is set to 5 kV and 30 kV, respectively. Table S1 summarizes the most relevant fabrication steps and conditions.

The process begins by selecting a clean region on the Bi_2Se_3 crystal using the SEM. To protect the chosen area for device fabrication from ion irradiation damage, a Pt layer is deposited [Fig. 1(a)]. Initially, a 12 µm × 6 µm rectangle of 300 nm nominal height is deposited *via* FEBID, using a current of 6.4 nA (volume per dose of $10^{-2}\mu m^3/nC$) with the stage horizontal, at 0º. Once this step is completed, the stage is tilted to 52º, to have the surface of the crystal facing the FIB perpendicularly. A second layer of the same area and 1 µm nominal height is then deposited by FIBID using current of 0.23 nA (volume per dose of 0.5 $\mu m^3/nC$). These current values are chosen to optimize the material deposition while minimizing the deposition time.

Continuing with a stage tilt of 52º and a current of 2.5 nA (1000 µs dwell time), FIB milling is performed next to the four sides of the rectangular Pt deposit to create trenches. Four trenches will be milled in total, two next to the long edges of the Pt deposit and two at the short ones. When milling perpendicularly, a slanted profile of the walls may form as the hole deepens. To mitigate this effect when creating the trenches at the longer sides of the rectangle, the bottom and upper trenches shown in Fig. 1(b) are milled at 55º and 49º, respectively. The milled regions need to be sufficiently wide and deep to allow cutting at an appropriate depth, ensuring there is enough material to later shape the crystal into its final shape. To complete the two remaining trenches, the areas next to the short sides are milled at 52º leaving an appropriate distance between the cut and the Pt deposit with the aim of having a grabbing spot for the nanomanipulator in future steps. Figure 1(c) displays a micrograph of the crystal after the milling of the four trenches is finished.

For the undercut, the stage is returned to its horizontal position [see Fig. 1(d), (e)]. The undercut is performed by FIB milling with a rectangle pattern of 0.35 µm × 13 µm until the SEM shows that the material has been fully cut. The left side cut is only partially completed before inserting and fixing the nanomanipulator [Fig. 1(f)] using Pt FIBID preventing any movement of the crystal until it is secured for transportation. Finally, the cut is completed, and the sample is transferred to a TEM grid for polishing.

Removal of Pt coating and thinning of the crystal slab

In this section, the procedure of shaping the extracted piece of Bi_2Se_3 into a slab of the desired dimensions is described.

The crystal piece, which was attached to the nanomanipulator with its Pt-covered surface oriented horizontally [Fig. 2(a), (b)], is adhered to the 90º-tilted grid (stage at 0º). First, Pt FEBID is used to make the bond, as the orientation of the electron beam is perpendicular at this position. Subsequently, Pt FIBID is applied to strengthen it. In this way, it is glued to the grid with the same orientation as a standard TEM lamella would have. Using FIB, the nanomanipulator is detached from the sample and subsequently withdrawn. After tilting the stage to 52º, the edges of the Pt deposit are milled at low currents (first at 80 pA and later at 24 pA, 1000 ns dwell time) to give the crystal a clean profile at the sides.

Then, the process chamber is opened and the grid holder is positioned vertically in its standard orientation, so the electron beam strikes the upper side of the still-covered-with-Pt crystal piece when the stage is at 0º. Note that this step could be avoided with the use of pre-tilted sample holders, improving the quality of the final devices by preventing unnecessary exposure of the crystal to unprocessed gases. To remove the Pt protective coating, the stage is rotated so that, when tilted to 52º for FIB milling, the Pt-coated surface faces the SEM. The stage is then tilted to 52.5º instead of 52º to avoid the formation of slanted profiles. A current of 2.5 nA is applied until only a thin layer of Pt remains. To avoid damaging the material, the current is reduced first to 80 pA and lastly to 24 pA to smoothen the now exposed crystal surface [Fig. 2(c)].

This process is repeated to the opposite face of the crystal, thinning it until the desired thickness is reached [Fig. 2(d)]. Once the polishing is done, exposure to irradiation is minimized to prevent contamination and damage on the Bi_2Se_3 crystal.

Contacting the crystal slab to the chip

To transport the crystal slab to the chip, the process chamber is opened for the last time and the grid holder is returned to its original position, so the sample is placed horizontally once again (this step could have been avoided with pre-tilted sample holders). The nanomanipulator is inserted and fixed to the sample following the method described previously. After detaching the slab from the grid *via* FIB milling, it is moved to the chip and placed at the center of the prepatterned gold leads [Fig. 2(e)]. With the stage kept horizontal, two Pt deposits, each 350 nm wide and with a nominal height of 500 nm, are deposited on the side exposed to the ion beam *via* FIBID. This is done at an angle to fix the slab to the chip, overcoming their height mismatch (Au contacts and the crystal slab have a height

of 50 nm and 800–1000 nm, respectively). These contacts will serve as voltage contacts during subsequent electrical transport measurements after they are connected to the gold leads in a later step. The nanomanipulator is then detached by FIB milling and withdrawn. Next, by rotating the stage around its perpendicular axis at a 0º tilt, the remaining fixing Pt deposits are grown by FIBID: two thin deposits opposite the previously grown ones, and two wider (2 µm) ones that will later be

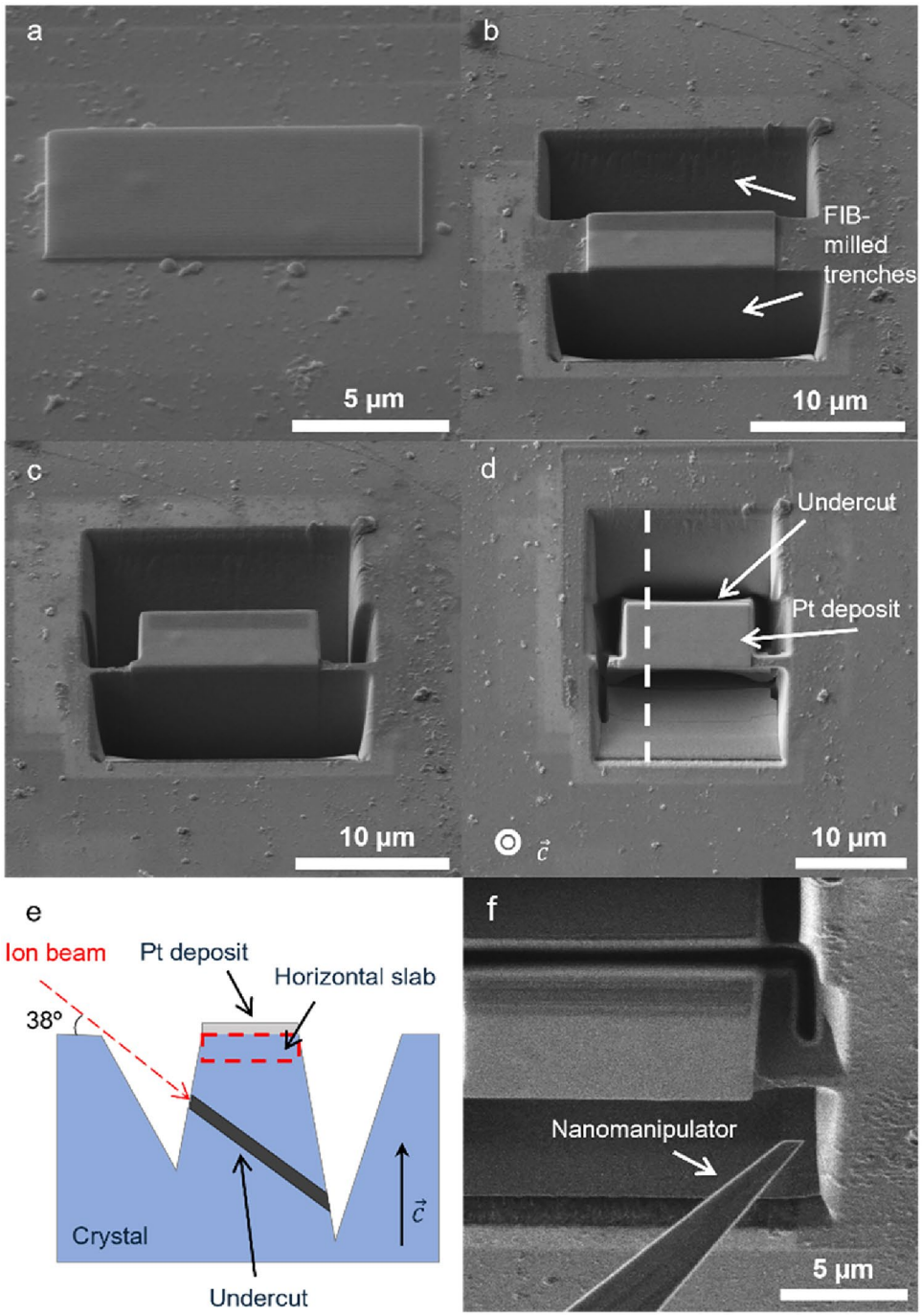

Figure 1. SEM micrographs of the fabrication process showing: (a) the Pt deposited by first FEBID and subsequently by FIBID covering the selected region of the Bi_2Se_3 single crystal for extraction, (b) the extraction area with the first two FIB-milled trenches, (c) the sample with the final side trenches milled and (d) the milled trenches and the undercut, where the dashed line indicates the direction of the cross-section scheme in figure (e). (e) Cross-section scheme along the dashed line in (d) showing the horizontal slab to be extracted. (f) FIB micrograph of the nanomanipulator approaching the grabbing point of the cut crystal slab. Image taken at an angle to observe the undercut.

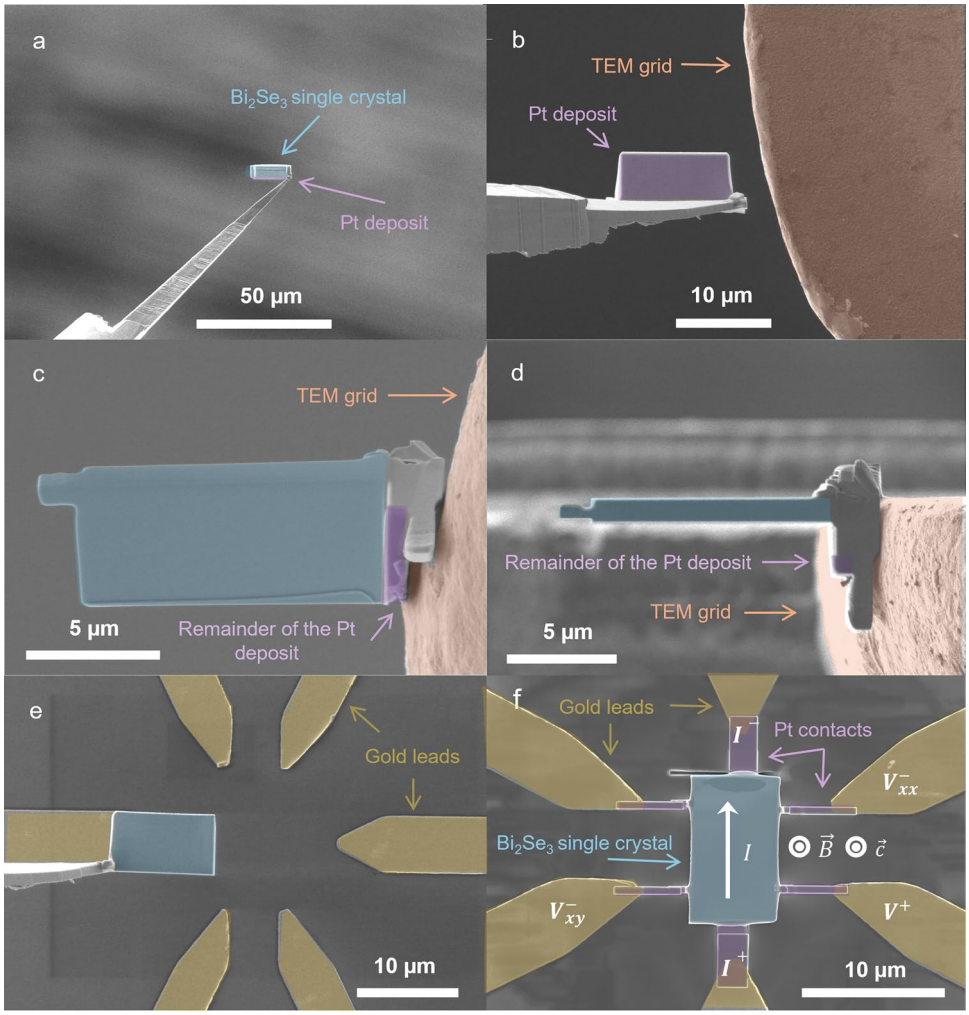

Figure 2. Colored micrographs of the fabrication process: (a) FIB micrograph showing the transportation of the extracted Bi_2Se_3 (blue) with the Pt deposit (purple) piece to the TEM grid. SEM micrographs representing (b) the sample next to the TEM grid (orange). (c) Thinning process done by the FIB and simultaneously monitored by SEM. (d) Final thickness of the polished crystal slab. (e) Single crystal slab transported to a silicon dioxide chip with gold leads (yellow). (f) Final device, with FIBID-deposited Pt contacts connecting it to the gold leads on the chip.

bonded to the gold leads for current injection. It is important to ensure that the contacts placed opposite each other are correctly aligned to prevent magnetoresistance contributions in subsequent Hall measurements during magnetotransport characterization.

Finally, these Pt deposits are connected to the gold leads by depositing platinum rectangles *via* FIBID at a 52° tilt [Fig. 2(f)].

Results and discussion

This section shows some results from magnetotransport measurements for two samples fabricated using method 2 (denoted by H for 'Horizontal') and their comparison to the results obtained in microcrystals fabricated following method 1 (denoted by V for 'Vertical').

For H samples, the fabrication process is designed to have the crystal orientated in a way that the electrical current flows perpendicular to its $\vec{c}$ axis whereas the magnetic field is parallel to this axis. In V samples it is the opposite, $\vec{c}$ axis is perpendicular to the magnetic field and parallel to current flow (Fig. 3). Therefore, to prove the utility of the method, which enables choosing the orientation that suits best the application of the device, a comparison between the magnetotransport properties of both kinds of samples will be discussed below.

We have performed longitudinal resistivity ρ_{xx} and Hall resistivity ρ_{xy} measurements using a four-probe setup at a temperature of 2 K. The electrical current used for characterization has been chosen to minimize the noise in the resistance measurements. V1 and V2 samples where characterized employing 20 µA and 1 µA, respectively, while a current of 10 µA was applied to horizontal samples.

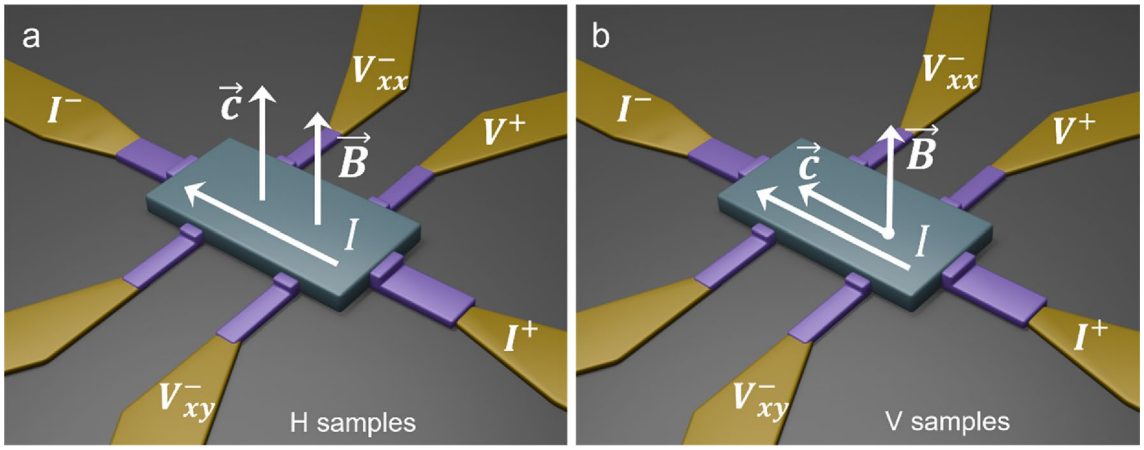

Figure 3. Computer-generated images showing a schematic of the orientation of the out-of-plane crystal axis and the applied magnetic field on H (method 2) and V (method 1) samples: (a) In H samples $\vec{B}$ and the $\vec{c}$ are perpendicular to both the slab surface and the direction of the current flow. (b) In V samples, $\vec{c}$ is parallel to the surface and to the direction of the current flow, while the magnetic field is applied perpendicularly.

Figure 4(a) displays the percentual change of longitudinal resistivity or perpendicular magnetoresistance (MR) as a function of the magnetic field, applied perpendicularly to the surface, calculated as

$$MR\% = \frac{\rho_{xx}(B) - \rho_{xx}(0)}{\rho_{xx}(0)} \times 100$$

MR% is not saturating for every sample measured up to 10 T. The relative change in resistivity when sweeping the magnetic field from 0 to 10 T is small in these samples, with a variation below 4% in both cases. This value is slightly lower than those reported in literature, which vary depending on the thickness, decreasing below 10% with increasing thickness.[17,18] Most of the MR data on H samples are reported on thin films, therefore our values are expected to be lower. V devices also showcase a low change in resistivity, nearly 1% for every sample, which is consistent with previously reported data along this crystal orientation.[13] Therefore, no big differences are observed in terms of magnetoresistance between both types of samples. One thing to notice is that the MR% curve corresponding to H2 is noisier and presents a negative MR% at low fields. This is due to a high resistivity value at 0 T, something we attribute to the noise generated by a bad contact of the aluminum wires bonding the PPMS's puck to the gold leads on the chip at low fields.

The biggest difference appears when studying the dependence of the Hall resistivity with B. In both cases it is linear with a negative slope [Fig. 4(b)], which indicates the presence of a single band of n-type carriers. By applying Drude model we can calculate the density of carriers n and the carrier mobility μ through the expressions:

$$n = -\frac{1}{eR_H}$$

$$\mu = \frac{1}{en\rho_{xx}}$$

where e is the elementary charge, R_H is the slope of the Hall resistivity curve and ρ_{xx} is the longitudinal resistivity at $B = 0T$. Table S2 summarizes the results of applying Drude model to the data from H and V samples. V samples exhibit higher resistivity compared to H samples. Charge carrier density is a factor of two higher in V samples than in H samples and their mobility differs by a factor of five. We attribute these variations in transport properties to the crystalline structure of Bi_2Se_3. In H samples, the current flows through the crystal planes, where atoms are covalently bonded. In contrast, in V microcrystals, electrons move across the Van der Waals bonds that connect different crystal planes. These weaker bonds increase the resistivity of V samples, whereas the stronger atomic connections in H samples facilitate electron transport and enhance mobility.

The differences in behavior between samples of the same type may be attributed to small structural variations in the regions of the crystal from which the slabs were extracted. The relatively small dimensions of the device can make it more susceptible to impurities, affecting its transport properties. Additionally, ion implantation and irradiation-induced damage during the fabrication process can alter the chemical and structural properties of the crystal, contributing to these variations in behavior among samples of the same type.[19] Despite these effects, there is a notable difference in the operation of the two kinds of devices, based on microcrystals extracted in perpendicular crystallographic orientations.

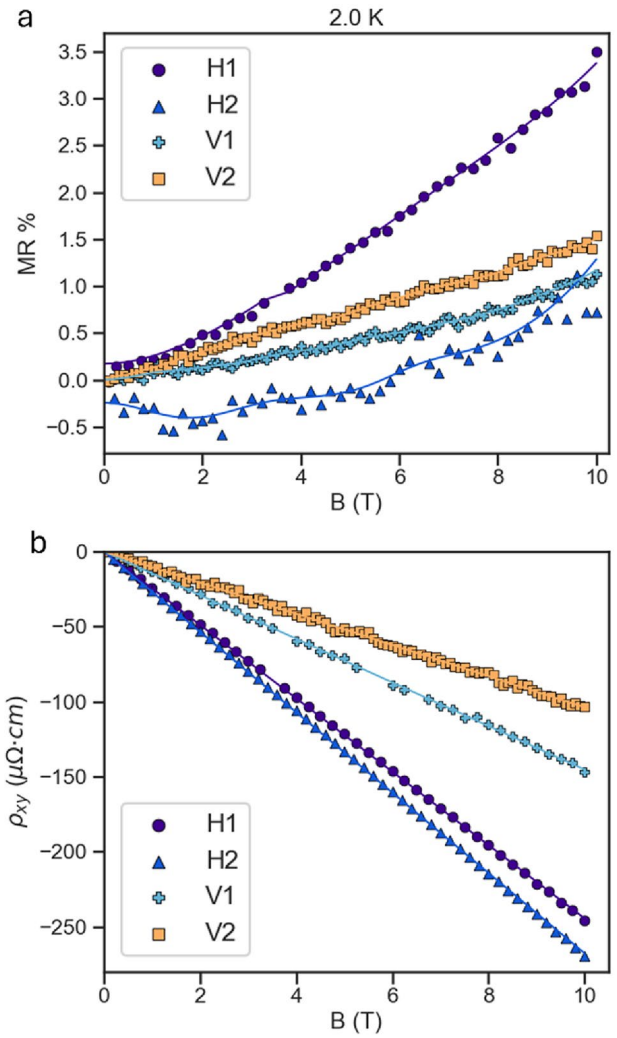

Figure 4. Magnetotransport measurements for different H and V samples at 2 K. Horizontal samples were measured using a current of 10 μA, while V1 and V2 were characterized using 20 μA and 1 μA, respectively. Standard deviation for H1, V1 and V2 is below 0.08% of the measurement for each point. For H2 it is below 0.4%. (a) Perpendicular magnetoresistance as a function of the applied magnetic field. Experimental data is shown along with a guide line obtained by a smoothing of the data using a rolling average. (b) Hall resistivity as a function of the applied magnetic field, with the continuous line representing a linear fit.

Conclusion

The fabrication method we propose, which has been demonstrated using Bi_2Se_3 as a model material, is designed to study transport properties in microcrystals extracted from bulk single crystal materials across different crystalline orientations. This approach enables selection of the direction of the electrical current flow through the lattice, benefiting from the advantages of a system integrating a SEM and a FIB, providing in situ control of the fabrication process, with real-time monitoring and manipulation of the samples.

To illustrate the utilization of this method we have compared magnetotransport measurements on Bi_2Se_3 single crystal devices with two different crystalline orientations. Longitudinal resistivity and Hall resistivity were measured at 2 K, using a four-probe setup. Devices called *H* were fabricated following method 2, the proposed new method, having the current flow perpendicular to the $\vec{c}$ axis and the applied magnetic field parallel to it. Samples referred to as V, were fabricated following the standard method (method 1), with current flow parallel and magnetic field perpendicular to the $\vec{c}$ axis. Magnetoresistance variations are small in both sample types, however, Hall resistivity measurements show differences. While both samples exhibit a linear negative slope, there are differences in a factor of five in resistivity and mobility of the charges. We attribute this to the crystalline structure of Bi_2Se_3. In H samples, current flows through the crystal planes, where atoms are covalently bonded, facilitating transport of electrons and therefore have a higher mobility and lower resistivity. In V samples, electrons travel through different layers bonded through Van der Waals forces, weaker links, thus reducing conductivity.

Additionally, structural variations, fabrication-induced damage, and impurities may contribute to variations among samples of the same type. Nonetheless, despite these effects, this study shows utility and advantages of the fabrication method, which can be applied to any conductive single crystal that is stable under FIB irradiation, evidencing differences in transport properties between both types of microcrystals with different crystallographic orientations. The development of this fabrication process is part of our efforts to develop the existing techniques for single crystal extraction using FIB technologies for their characterization or implementation in nanofabrication of more complex devices, such as the achievement of superconducting proximity effect on a topological insulator crystal.[13]

Acknowledgments

The authors are grateful to R. Gracia-Abad, who had an important contribution to the development of method 1, on which this method was built. The authors would like to thank the Laboratory for Advanced Microscopies (LMA) and the Institute of Nanoscience and Materials of Aragón (INMA), from CSIC–Universidad de Zaragoza, for providing access to their instruments and expertise. The authors are grateful to the ELECMI network for granting free access through a competitive call to the Helios 650 system with project ELC385-2023. Technical support from the LMA technicians at Universidad de Zaragoza is acknowledged, with special thanks to L. Casado for her assistance with the nanofabrication procedures involving the Dual Beam system. Additionally, the Physical Measurements Service from *Servicio General de Apoyo a la Investigación* (SAI) at the University of Zaragoza is also acknowledged.

Author contributions

A.S. contributed to the design of the experiment, performed the experiments, analyzed the data and wrote the first version of the manuscript. S.S. and J.M.D.T. obtained the funding, supervised the work, contributed to the design of the experiment, to the data analysis and to the final version of the manuscript. G. B. obtained the funding and provided the Bi_2Se_3 single crystal.

Funding

Open Access funding provided thanks to the CRUE-CSIC agreement with Springer Nature. The authors acknowledge grant PID2020-112914RB-I00 and PID2023-146451OB-I00, funded by MCIN/AEI/https://doi.org/10.13039/501100011033, and CSIC through Research Platform PTI-001. The doctoral fellowship (A. S. H.), PRE2022-103314, associated with project CEX2021-001144-S-20–9, also from CSIC, is also acknowledged. The work at the University of Warwick was supported by EPSRC, UK, through grant EP/T005963/1.

Data availability

Data are available under reasonable request.

Declarations

Conflict of interest

Authors declare that there is no conflict of interest.

Supplementary Information

The online version contains supplementary material available at https://doi.org/10.1557/s43579-025-00719-8.

Open Access

References

1. F. Y. Yang *et al.*, Science (1979) **284**, 1335 (1999).
2. M. Ziese, H.J. Blythe, J. Phys. Condens. Matter **12**, 13 (2000)
3. P.J.W. Moll, Annu Rev Condens Matter Phys **9**, 147 (2018)
4. K. Höflich et al., Appl. Phys. Rev. **10**, 41311 (2023)
5. S. Abhirami et al., Phys. Chem. Chem. Phys. **26**, 2745 (2024)
6. Y.L. Shabelnikova, S.I. Zaitsev, J. Surf. Invest. **16**, 605 (2022)
7. J.M. De Teresa et al., Micromachines **2019**(10), 799 (2019)
8. D.S. Gianola et al., Rev. Sci. Instrum. **82**, 63901 (2011)
9. J. Mayer et al., MRS Bull. **32**, 400 (2007)
10. P.J.W. Moll et al., Nat. Commun. **6**, 6663 (2015)
11. J. Diaz et al., Nat. Commun. **15**, 4585 (2024)
12. E. Mikheev et al., Nano Lett. **22**, 3872 (2022)
13. R. Gracia-Abad et al., Sci. Rep. **14**, 24294 (2024)
14. Y. Xia et al., Nat. Phys. **5**, 398 (2009)
15. R. Gracia-Abad et al., Nanomaterials **11**, 1077 (2021)
16. Y. Yan et al., Sci. Rep. **3**, 1264 (2013)
17. P.H. Le et al., Chin. J. Phys. **91**, 857 (2024)
18. P. Singha et al., J. Appl. Phys. **135**, 25001 (2024)
19. R. Gracia-Abad et al., Materials **16**, 2244 (2023)